Chapter 2

STABILITY OF SLENDER INVERTED FLAGS

John E Sader, Cecilia Huertas-Cerdeira, and Morteza Gharib. Stability of slender inverted flags and rods in a uniform steady flow. *Journal of Fluid Mechanics* 809:873–894,2016.

The main findings highlighted in Chapter 1 correspond to inverted flags of relatively high aspect ratios (AR>1). Above that threshold, the general features of the flag's behavior are consistent independently of this parameter. Variations with aspect ratio have been reported, however, in the values of the critical velocities, as well as the amplitudes and frequencies of flapping. Preliminary experimental results by Cossé et al. (2014) and a more detailed follow-up in Sader et al. (2016a) indicated that the critical value of the non-dimensional velocity, κ, at which the flag enters the flapping regime increases as aspect ratio is decreased, while the value of κ at which the flapping motion disappears remains constant for all aspect ratios. Similar results were numerically obtained at Re=200 by Tang et al. (2009), who observed, nonetheless, a small variation in the values of κ at which flapping ceases. Tang et al. (2015) reported an approximately constant overall maximum flapping amplitude, A, although the velocity at which higher aspect ratios reached this value was lower, showing a wider maximum-amplitude plateau. A substantial decrease in Strouhal number was additionally reported as aspect ratio decreased.

As was highlighted in Chapter 1, the onset of flapping of high-aspect-ratio inverted flags is caused by a divergence instability. Sader et al. (2016a) presented a theoretical analysis that is able to predict the onset of flapping for flags of aspect ratio AR>1. Their model followed the steady version of the theory developed by Kornecki et al. (1976) which considers two-dimensional, inviscid, incompressible flow combined with the equilibrium equation of an elastic plate and the corresponding boundary conditions. The divergence velocity is then computed making use of the Rayleigh quotient. The analytic formula, valid for varying aspect ratios, was obtained by correcting this infinite aspect ratio value with a factor of $1 + \frac{2}{AR}$, as derived from Prandtl's lifting line theory making the assumption of a negligible Glauert coefficient (Anderson Jr, 2010; Glauert, 1983). The formula obtained reasonable agreement with experiments for aspect ratios up to 1. Formally, Prandtl's lifting line theory is an asymptotic formula for high aspect ratios. It is generally considered to hold closely for AR>4 (Bollay, 1939), with vortex lattice methods being used for AR>1. At smaller aspect ratios the edge vortices produce non-linear effects that cannot be captured by this linear theory. The formula obtained by Sader et al. (2016a) strongly overpredicts the transition velocity of inverted flags of these small aspect ratios, consistent with a vortex lift mechanism that enhances the lift on the flag, therefore reducing the critical velocity.

The objective of this chapter is to characterize the behavior of slender inverted flags (AR<1). It is important to note that the experimental results by Cossé et al. (2014) and Sader et al. (2016a) established the existence of a flapping regime for AR>0.2 only. Under that threshold, the flag transitions directly from oscillating around a small deflection position to oscillating around a large deflection equilibrium. Consequently, the theoretical analysis presented in Section 2.1, developed by collaborators at the University of Melbourne for the limit of AR$\rightarrow$ 0, addresses the existence and stability of steady state equilibria only. The experiments presented in Section 2.2, give further insights into the effect of a finite, but small, aspect ratio and the system's dynamics.

2.1 Theory

A theoretical framework for the stability of inverted flags in the limit of zero aspect ratio was developed by Prof. John Sader and is summarized below. A more extensive description can be found in Sader et al. (2016b). The theory is based on the result by Bollay (1939), who considered the effect of edge vortices that trail at an angle to the free-stream velocity, obtaining a non-linear theory for the lift of flat plates of AR<1. In the limit of zero aspect ratio, the normal force coefficient becomes

$$C_N = 2\pi \sin^2 \alpha \tag{2.1}$$

with α the angle of attack of the plate. The equilibrium equation for a beam undergoing large-deformation pure bending (Landau and Lifshitz, 1970) is given by

$$EI \frac{d^2\theta(s_*)}{ds_*^2} = -\mathbf{n}(s_*) \cdot \int_{s_*}^{L} \mathbf{F}(l_*)\, dl_*, \tag{2.2}$$

where $\theta(s_*)$ is the local rotation angle of the beam, s_* (and the equivalent integration variable l_*) is the dimensional arc-length along the beam ($s_* = 0$ at the clamped end) as defined in figure 2.1. E is the Young's modulus of the beam, I is its areal

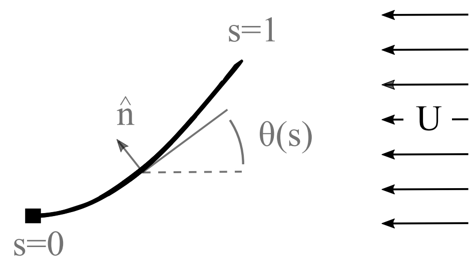

Figure 2.1: Definition of local rotation angle of the beam, $\theta(s)$, and arc-length along the beam, s.

moment of inertia, **F** is the local applied force per unit length and **n** is the local unit normal to the beam's axis at position l_*. Equation (2.2) satisfies the required zero force condition at the free end of the cantilever($s_* = L$).

Combining equations 2.1 and 2.2, the equilibrium equation for the slender inverted flag becomes

$$\frac{d^2\theta}{ds^2} = -\kappa' \int_s^1 |\sin\theta(l)| \sin\theta(l) \cos(\theta(s) - \theta(l))\, dl, \tag{2.3}$$

where the dimensionless arc-length, $s \equiv s_*/L$ (and $l \equiv l_*/L$), is now used. The dimensionless velocity κ' is the beam equivalent of κ as defined in Section 1.2, where the flexural rigidity has been substituted by that of a beam of rectangular cross section $D' = Eh^3/12$. The absolute value in the right-hand side is included to account for the inherent symmetry in the flag's deflection. The corresponding boundary conditions are

$$\theta(0) = \left.\frac{d\theta}{ds}\right|_{s=1} = 0, \tag{2.4}$$

Equation 2.3 can be solved numerically, using a finite difference discretization combined with a shooting method, where the angle at the free end of the cantilever, $\theta_{end} = \theta(1)$, is adjusted to match the required clamp condition, $\theta_{clamp} = \theta(0) = 0$ (Luhar and Nepf, 2011). The obtained results are represented in figure 2.2 and show the existence of a saddle-node bifurcation, in contrast to the divergence instability present in the large-aspect-ratio case. The variable employed is θ_{end}, which is equivalent but not equal to the deflection angle, θ. For small values of κ', a single solution to equation 2.3 exists. It corresponds to the zero deflection equilibrium ($\theta_{\text{end}} = \theta_{\text{clamp}} = 0$). As κ' is increased, a second solution, corresponding to the deflected equilibrium $\theta_{end} = 66.7°$, appears and further divides into two distinct

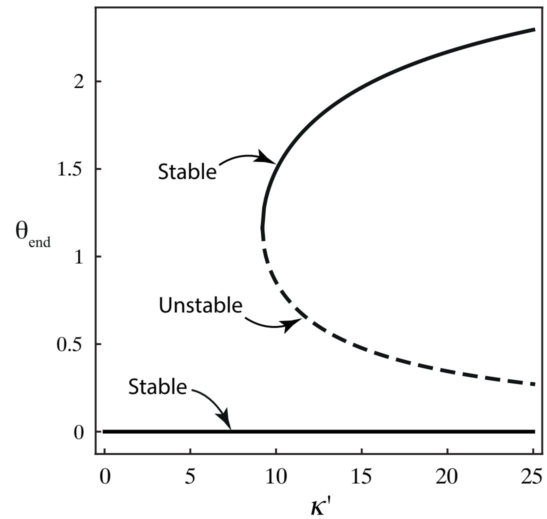

Figure 2.2: Theoretical bifurcation diagram of the inverted flag's free end angle θ_{end} vs. normalized flow speed κ' in the limit AR $\rightarrow$ 0. Solid curves correspond to stable equilibria, dashed curves correspond to unstable equilibria. Only positive angles are shown – negative angles have symmetric behavior.

equilibria for higher values of κ'. The critical κ' at which this saddle-node bifurcation occurs is $\kappa'_{crit} = 9.205$. The stability of these equilibria can be deduced from the fact that the aerodynamic force does not present a linear term (equation 2.1), and therefore the zero-deflection equilibrium must necessarily be linearly stable.

The results in figure 2.2 have been obtained using a steady aerodynamic force and do not account for the unsteadiness of the separated flow. Inverted flags of AR<0.2 do not present large-amplitude flapping, and therefore, as will be shown experimentally in Section 2.2, the unsteady effects are limited to generating small amplitude oscillations around the equilibria. In order to gain some intuition on the system's stability and dynamics, a simplified rigid flag model, that reduces the flag motion to a single degree of freedom, can be employed. The equation of motion of a rigid beam that is mounted on a torsional spring at its trailing edge is given by

$$\frac{d^2\bar{\theta}}{dt^2} + \frac{1}{Q}\frac{d\bar{\theta}}{dt} + \bar{\theta} - \bar{\kappa}\left|\sin\bar{\theta}\right|\sin\bar{\theta} = F(\bar{\theta}, t), \tag{2.5}$$

where $\bar{\theta}$ is the beam's rotation angle, $\bar{\kappa}$ is analogous to the non-dimensional flow speed and accounts for the spring's constant, Q is the quality factor, t is scaled time and $F(\bar{\theta}, t)$ is an unspecified external applied force due to the unsteady hydrodynamic force arising from vortex shedding and any turbulence in the impinging flow. The potential energy of the steady system (third and fourth terms) can be calculated and provides insight into the competing elastic and steady aerodynamic forces. It is given by

$$V(\bar{\theta}) = \frac{1}{2}\bar{\theta}^2 - \frac{\bar{\kappa}}{2}\left|\bar{\theta} - \frac{1}{2}\sin 2\bar{\theta}\right|, \tag{2.6}$$

and is plotted in figure 2.3. In this figure, the stationary points correspond to equilibrium solutions and agree with the bifurcation diagram presented in figure 2.2. For small values of $\bar{\kappa}$, the zero deflection equilibrium is solely present. As $\bar{\kappa}$ is increased a saddle-node bifurcation occurs and an unstable (potential maximum) and stable (potential minimum) equilibria appear. This simplified model notably shows the basins of attraction of the equilibria. At $\bar{\kappa}$ slightly above the bifurcation velocity, the potential well of the stable deflected equilibrium is shallow and the energy required to reach the unstable equilibrium from it is small; any small perturbation will lead the flag back to the stable zero-deflection equilibrium. In contrast, at high values of $\bar{\kappa}$ the potential well of the deflected equilibrium is steep and the energy required to exit the zero-deflection equilibrium is small; perturbations will lead the flag towards the deflected equilibrium. This explains why, despite the zero-deflection equilibrium being always stable, all experimental investigations up to date have reported that increasing wind speed results in the flag transitioning from the zero-deflection state to the deflected state. The intermittency inherent to low aspect ratio inverted flags is further analyzed in Section 2.2.

The normalized velocity κ' at which inverted flags in the AR $\rightarrow$ 0 limit undergo a saddle-node bifurcation can be translated to the large aspect ratio variable κ as follows

$$\kappa_{small} = 9.205(1 - \nu^2) \tag{2.7}$$

with ν the Poisson ratio of the flag. The theory presented by Sader et al. (2016a) for the AR $\rightarrow \infty$ limit predicted a divergence instability at a value of

$$\kappa = \kappa_{large}\left(1 + \frac{2L}{H}\right) \tag{2.8}$$

where

$$\kappa_{\mathrm{large}} = 1.85. \tag{2.9}$$

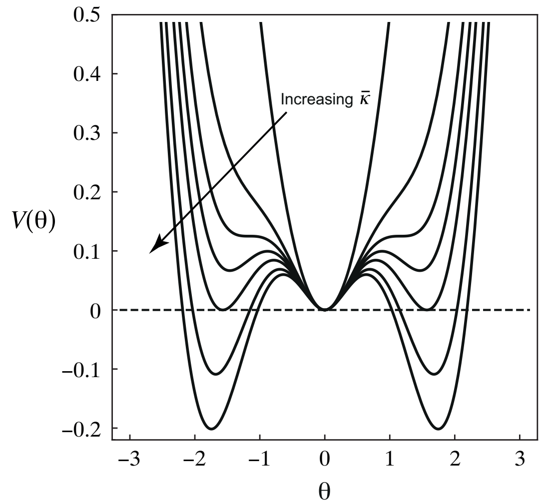

Figure 2.3: Potential energy function, $V(\bar{\theta})$, of the rigid beam model system for $\bar{\kappa} = 0, 1.2, 1.38, 1.48, \pi/2, 1.7, 1.8$ (increasing from center outwards); saddle-node bifurcation occurs at $\bar{\kappa} = 1.38$. Both positive and negative angles are given.

These two equations for the asymptotic limits can be combined using a Padé approximant to obtain a formula that can predict the end of the straight regime for flags of all aspect ratios

$$\kappa \approx \kappa_{\text{large}} \frac{\kappa_{\text{small}} + \left(\kappa_{\text{small}} - \kappa_{\text{large}}\right) \frac{H}{2L}}{\kappa_{\text{large}} + \left(\kappa_{\text{small}} - \kappa_{\text{large}}\right) \frac{H}{2L}}, \tag{2.10}$$

Because the zero-deflection regime of the low aspect ratio limit is always stable, and the flag only deflects as its basin of attraction becomes sufficiently small, formula 2.10 should be taken as a lower bound. It is plotted, together with both asymptotic theories and experimental results by Sader et al. (2016a) in figure 2.4 and shows good agreement throughout.

The possible existence of multiple equilibria, as predicted theoretically in this section, was explored experimentally. These measurements aim to test for the presence of these equilibria, as well as give insight into the flag's dynamics and the behavior of flags of small but finite aspect ratios.

2.2 Results

Multiple equilibrium states of the flag

The new measurements verify the existence of multiple equilibrium states, as predicted theoretically in Section 2.1. This theory does not, however, account for

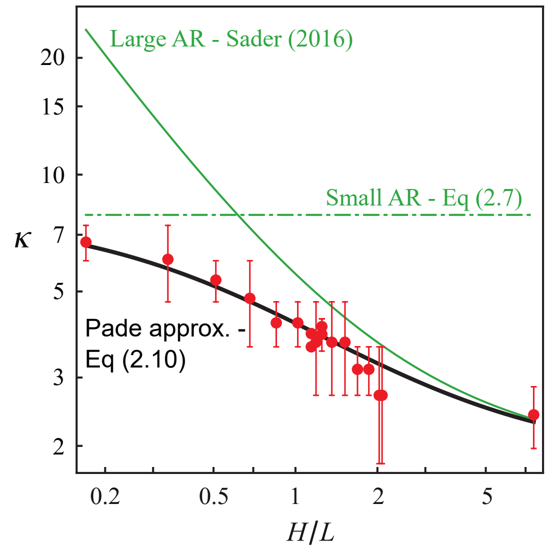

Figure 2.4: Comparison of measurements and theoretical predictions for the critical normalized flow speed at bifurcation, as a function of aspect ratio, H/L. Equation (2.8) [upper curve, large aspect ratio solution], (2.7) [horizontal line, small aspect ratio solution] and (2.10) [lower curve, globally valid Padé approximant].

dynamic effects, which modify the behavior of the flag. For the smallest aspect ratios, $H/L < 0.2$, the flag was experimentally observed to oscillate with small amplitude around the stable equilibrium positions. In those cases, the deflected stable equilibrium position, presented in figure 2.5, was measured by taking the average of a 30 s time series. Large-amplitude flapping occurs for aspect ratios $H/L > 0.2$ (Sader et al., 2016a). In these cases, the flag was damped to observe a deflected equilibrium; this was achieved by lightly touching the flag with a thin rigid pole.

Existence of an unstable deflected equilibrium was assessed as follows. The initial position of the flag was adjusted by quasi-statically pushing it from the stable deflected equilibrium position towards the zero-deflection position using a thin and rigid pole. Presence of an unstable deflected equilibrium must then lead to rapid and unassisted movement of the flag from the deflected initial condition towards the zero-deflection equilibrium. The deflected shape of the sheet at the time of loss of contact with the pole is taken to be the unstable deflected equilibrium.

Figure 2.5 shows the measured angle of the cantilevered sheet's free end at the stable and unstable deflected equilibria. Measurements from several flags of varying small aspect ratios are presented, together with the theoretical predictions of Section 2.1. As the aspect ratio is reduced (left-to-right and top-to-bottom in figure 2.5), both the measured critical bifurcation flow speed κ'_{small} and the free end angle θ_{end} increase,

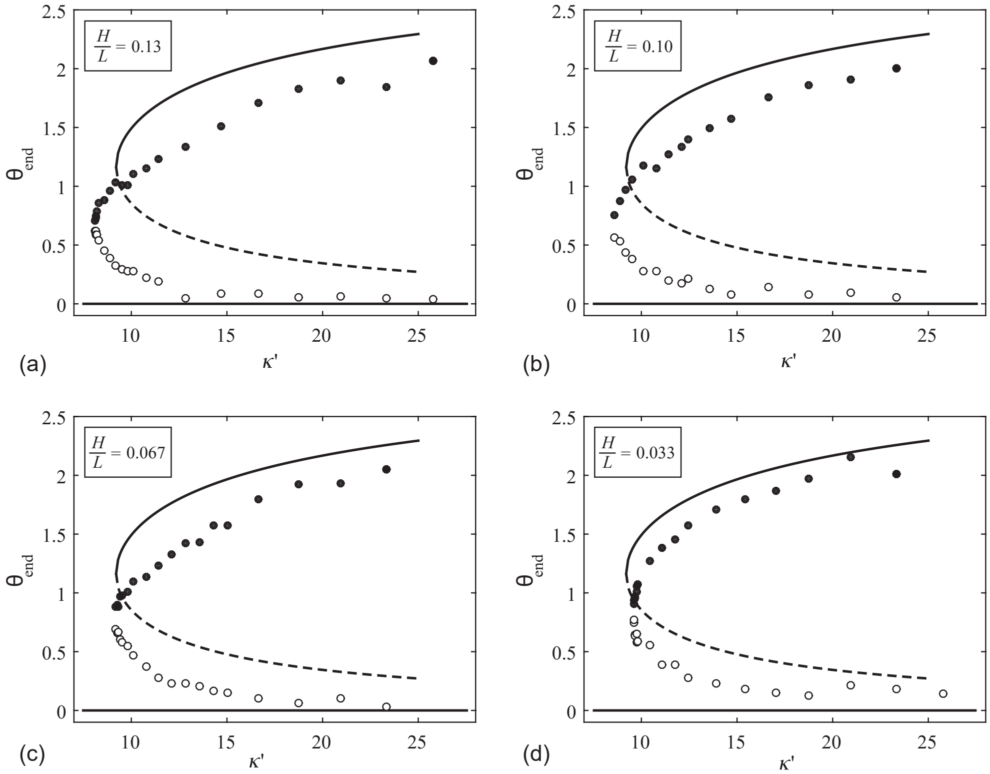

Figure 2.5: Measured free end angle, θ_{end}, at the stable (•) and unstable (◦) deflected equilibria for aspect ratios of (a) $H/L = 0.13$, (b) $H/L = 0.10$, (c) $H/L = 0.067$, (d) $H/L = 0.033$. Theoretical prediction using the $H/L \to 0$ asymptotic theory of Section 2.1 is given for stable (upper solid curve) and unstable (dashed curve) equilibria. Zero-deflection equilibrium position is shown for reference (horizontal solid line).

shifting towards the theoretical ($H/L \to 0$) curve of Section 2.1. While there are some differences, even at the smaller aspect ratios, the measurements clearly approach the theoretical asymptotic solution as H/L is reduced.

Interestingly, the measurements reported in figure 2.5 systematically underestimate the $H/L \to 0$ asymptotic theory. This may be due, in part, to twisting of the flag which is observed to always occur when the flag deflects from its zero-deflection equilibrium. This twisting deformation is shown in figure 2.6 and exhibits a commensurate downward displacement of the flag. Large deformation of elastic beams inevitably results in coupling between bending and torsion, if the load or beam is not perfectly symmetric about the beam's major axis (Landau and Lifshitz, 1970). Strikingly, every inverted flag studied here deforms in precisely the same manner — with the free end deflecting vertically downward in the gravity direction — demonstrating that gravity provides a symmetry break. When the flags are deflected sideways by applying a horizontal force with a stiff thin pole and the bank of fans are turned off, i.e., no flow, the large amplitude twisting shown in figure 2.6 is not observed, suggesting that the initial break in symmetry is small. The resulting small twist, however, appears sufficient to modify the aerodynamics of the flag such that an additional torsional aerodynamic force is generated, resulting in a large twisting deformation. This coupled bending/twisting deformation is expected to reduce the drag experienced by the inverted flag because the flag now presents an angled face to the incoming flow. Such drag reduction reduces the maximum deflection angle of the inverted flag for a given flow speed, consistent with the observations reported in figure 2.5. While non-linear coupling between bending and twisting under a gravitational load can be calculated, this complexity detracts from the principal aim of this study which is to describe the dominant stability mechanisms of slender inverted flags. The experimental angles reported in figure 2.5 are measured by observing the flag from above, and as such, they correspond to the projection of the deflection angle on the horizontal plane.

Bollay's 1939 calculations indicate that the normal force experienced by a rigid and flat blade of small but finite aspect ratio contains a term proportional to $\sin^2\theta$ and one proportional to $\sin 2\theta$. As such, a small but measurable linear lift component is expected, which may contribute to the observed differences between measurement and theory in figure 2.5. This mechanism acts in addition to the reduction in drag due to twisting, and its presence and strength are explored using independent measurements in Section 2.2.

Measurements by Sader et al. (2016a) found no evidence for the existence of the multiple equilibria reported in figure 2.5. However, their study focused primarily on flags of large aspect ratio, H/L. It is therefore important to determine the aspect ratio at which the multiple equilibria emerge. A systematic experimental investigation using the present setup reveals that these multiple equilibria occur only for $H/L < 1.7$. Figure 2.7 gives the measured bifurcation diagram, i.e., the stable and unstable equilibrium end angles, θ_{end}, as a function of the normalized flow speed, κ', for several aspect ratios, H/L, in this range.

The linear component of the hydrodynamic force described above, i.e., the $\sin 2\theta$ term, is expected to increase in strength with increasing aspect ratio. Unlike the limiting case of $H/L \to 0$ where the zero-deflection equilibrium is always linearly stable, this additional linear component will cause the zero-deflection equilibrium of finite aspect ratio flags to become linearly unstable at finite flow speed. This behavior

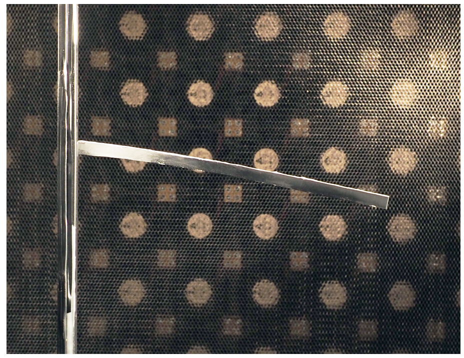

Figure 2.6: Photograph of slender inverted flag showing the combined flexural bending and twisting at large flow speeds, under the influence of gravitational and hydrodynamic loading; $H/L = 0.033$, $\kappa' = 16.6$. The bank of computer fans is visible with the flow direction out of the page. The flag is deflected strongly to the right relative to the flow direction, exhibiting a twist about its major axis together with commensurate bending in both the horizontal and vertical directions. The supporting aluminum bar is oriented in the vertical direction.

is evident in figure 2.7, where the unstable deflected equilibrium branch (dashed curves) crosses the zero axis, causing the zero-deflection equilibrium to become linearly unstable. The critical κ'-value at which this crossing occurs decreases as H/L is increased, as would be expected for an increasing linear component of the normal force. Indeed, this observed decrease in the unstable equilibrium's free end angle θ_{end} at bifurcation, with increasing H/L (see figure 2.7), is consistent with the large aspect ratio theory of Sader et al. (2016a): for large H/L, the deflected unstable equilibrium does not exist and a divergence instability of the zero-deflection equilibrium occurs.

Intermittent dynamics at moderate flow speeds

The rigid sheet model described by equation (2.5) does not explicitly account for the effects of nonlinear damping or unsteady hydrodynamic forces, such as those produced by vortex shedding and turbulence in the flow; these are lumped into the unspecified forcing term $F(\bar{\theta}, t)$. Therefore, it does not completely model the dynamics of the inverted flag. However, (2.5) does prove useful in gaining a qualitative understanding of the inverted flag's stability and dynamics. For small values of $\bar{\kappa}$, the secondary potential well at finite $\bar{\theta}$ (corresponding to the stable deflected equilibrium) is shallow; see figure 2.3. This suggests that residence at this minimum is energetically unfavorable and small fluctuations in the flow will drive the flag away from the stable deflected equilibrium. This behavior is now

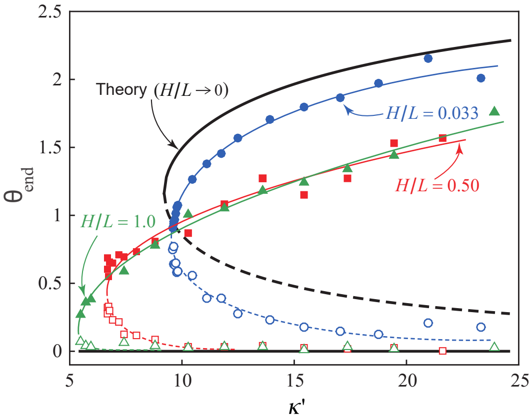

Figure 2.7: Measured free end angle, θ_{end}, of inverted flags at their stable (•) and unstable (∘) deflected equilibria as a function of the normalized flow speed, κ'. Measurements shown for flags of aspect ratios of $H/L = 0.033$ (blue circle), $H/L = 0.50$ (red square) and $H/L = 1.0$ (green triangle). To guide the eye, fit curves to these measured data points are provided for each aspect ratio. Theoretical prediction is given for the limiting case of $H/L \to 0$ (solid black curves: stable equilibria; dashed black curve: unstable equilibrium). Undeflected shape (zero angle) is the horizontal black line.

investigated experimentally.

Figure 2.8(a) shows the variation in time of the non-dimensional displacement of the flag's free end, A/L, for $\kappa' = 9.2$. This flow speed is just above the bifurcation point where the two deflected equilibria emerge in measurements. Initially, the flag fluctuates around the zero-deflection equilibrium. Using a thin and rigid pole, the flag is pushed (dashed red curve) to the stable deflected equilibrium position where it is released. The flag then resides at that position for finite time ($\approx$ 25 s) until it abruptly, and of its own accord, falls back into the zero-deflection position. This observation is consistent with the energetic picture in figure 2.3 where fluctuations in the flow are expected to result in intermittent dynamics.

As $\bar{\kappa}$ is increased in the model system, its deflected energy minimum depresses below the zero-deflection energy minimum; see figure 2.3. Physically, this lets small fluctuations drive the flag from the zero-deflection equilibrium towards the more energetically favorable deflected equilibrium. A measurement under this scenario is shown in figure 2.8(b), corresponding to a normalized flow speed of $\kappa' = 14.3$. The flag, initially oscillating around the deflected equilibrium, is forced (dashed red curve) with the thin pole to the zero-deflection position where it is again released. The flag then resides briefly ($\approx$ 3 s) at the zero-deflection position before returning suddenly and unaided to the deflected equilibrium position. The above-reported intermittency is expected to depend on fluctuations due to unsteady vortex shedding and on the level of turbulence in the impinging flow, with increased movement between multiple equilibrium states as the turbulence level is raised.

As mentioned above, the flag exhibits oscillations about both the zero-deflection ($A/L = 0$) and deflected ($A/L > 0$) equilibria in these measurements. The deflected equilibrium's oscillation amplitude is different in figures 2.8(a) and (b), with larger oscillations occurring at the lower flow speed (in figure 2.8(a)). This is expected because the energy minimum at the deflected equilibrium is shallower at the lower flow speed, as discussed above, allowing time-dependent fluctuations in the flow to more strongly perturb the sheet from this equilibrium position. The zero-deflection equilibrium exhibits reversed behavior, with larger oscillations being observed at the higher flow speed in figure 2.8(b). This is again explained by the energy landscape in figure 2.3, as the zero-deflection equilibrium's energy minimum is shallower at higher flow speeds — behavior opposite to that of the deflected equilibrium's energy minimum. Therefore, the observed oscillation amplitudes of the zero-deflection and deflected equilibria are entirely consistent with their intermittent dynamics discussed above.

Presence of a linear hydrodynamic lift force at finite aspect ratio

We now examine whether a linear lift force indeed exists for inverted flags of small but finite aspect ratio, as suggested by the results of Section 2.2. This is achieved by performing independent measurements of the natural resonant frequency of the inverted flags at their zero-deflection equilibrium positions, as a function of aspect ratio.

When a slender inverted flag is placed at its zero-deflection equilibrium at finite flow speed, it is observed to resonate with small amplitude; see figure 2.8. For such small amplitudes, the quadratic (fourth) term on the left hand side of the rigid sheet model system (2.5) — which holds formally in the limit $H/L \to 0$ — is small relative to the linear (third) term, provided $\bar{\kappa}$ is not large. The equation of motion for a damped harmonic resonator is then recovered. This equation depends on $\bar{\kappa}$ only through variations in the normalized damping coefficient, $1/Q$, and the external applied (hydrodynamic) force, $F(\bar{\theta}, t)$. These variations can both generally be considered small for small oscillation amplitudes. The resonant frequency of the flag is therefore weakly dependent on $\bar{\kappa}$ in this zero-aspect-ratio limit.

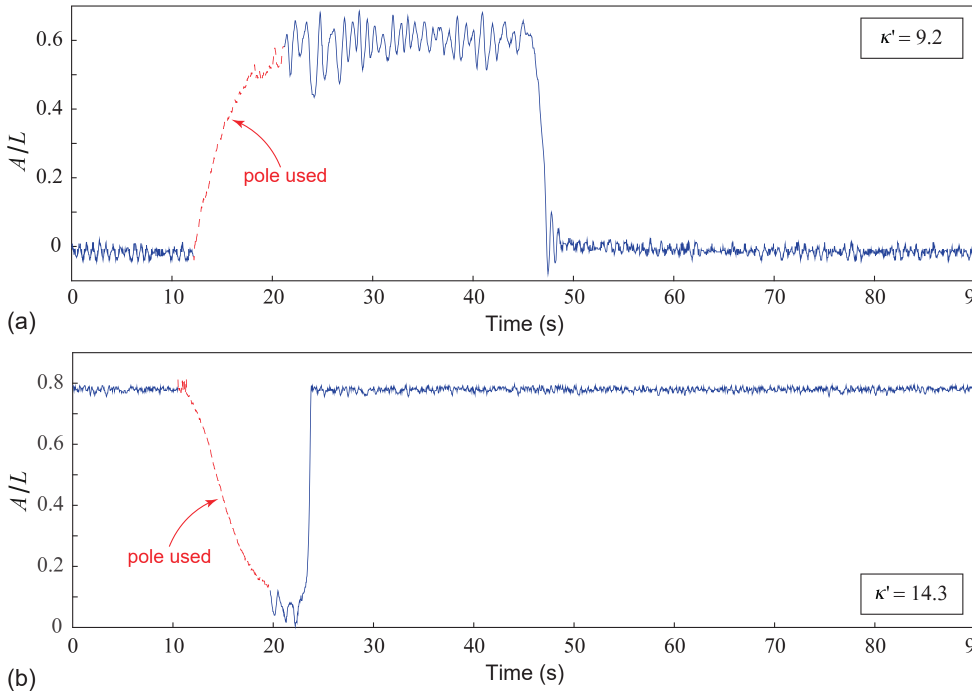

Figure 2.8: Measured dimensionless free end displacement A/L of an inverted flag as a function of time, for normalized flow speeds of (a) $\kappa' = 9.2$ and (b) $\kappa' = 14.3$. Aspect ratio $H/L = 0.067$. The flag is shifted to a different equilibrium using a thin rigid pole (red dashed curve) and then released.

For small but finite aspect ratio ($H/L \ll 1$), however, the hydrodynamic force on the rigid sheet includes a linear term, as discussed above (Bollay, 1939). In addition to the non-linear lift specified by Eq. (2.1) for a rigid slender blade, a linear normal lift force coefficient per unit length of the form $C_N = 2c \sin\theta \cos\theta$ arises, as discussed in Section 2.2. Here, $c = 0$ in the zero aspect ratio limit ($H/L \to 0$) and is an increasing function of aspect ratio. Equation (2.5) thus takes the modified form,

$$\frac{d^2\bar{\theta}}{dt^2} + \frac{1}{Q}\frac{d\bar{\theta}}{dt} + \bar{\theta} - c\bar{\kappa}\sin\bar{\theta}\cos\bar{\theta} - \bar{\kappa}\left|\sin\bar{\theta}\right|\sin\bar{\theta} = F(\bar{\theta}, t). \tag{2.11}$$

For small oscillations around the zero-deflection equilibrium, this equation can be linearized to give

$$\frac{d^2\bar{\theta}}{dt^2} + \frac{1}{Q}\frac{d\bar{\theta}}{dt} + (1 - c\bar{\kappa})\bar{\theta} = F(\bar{\theta}, t). \tag{2.12}$$

This shows that the resonant frequency of the rigid sheet system (and an inverted flag) of small but finite aspect ratio, H/L, varies as a function of the square root of $1 - c\bar{\kappa}$ and Q, which is weakly dependent on $\bar{\kappa}$. Since c increases with increasing aspect ratio, larger aspect ratio sheets are expected to display a more significant reduction in their resonant frequency with increasing $\bar{\kappa}$.

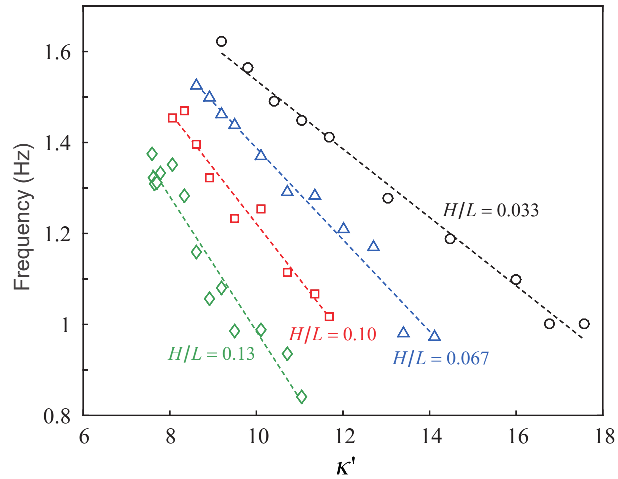

Figure 2.9: Natural frequency of oscillation of the zero-deflection equilibrium for inverted flags with aspect ratios of $H/L = 0.033$ (○), $H/L = 0.067$ (△), $H/L = 0.10$ (□) and $H/L = 0.13$ (◇). Linear fits to each data set are provided (dashed lines).

Figure 2.9 gives the measured oscillation frequency of the zero-deflection equilibrium for several flags, as a function of the normalized flow speed κ' and aspect ratio H/L. Although the dependence on κ' is not necessarily linear, a linear fit is provided to facilitate comparison. The measured rates of decrease in frequency are -0.15, -0.12, -0.10 and -0.075 Hz for aspect ratios of $H/L = 0.13$, 0.10, 0.067 and 0.033, respectively. This verifies the above physical picture: a linear lift force exists for finite aspect ratio and its magnitude increases with increasing aspect ratio.

A significant reduction in frequency as flow speed increases is observed even for the smallest aspect ratio of $H/L = 0.033$. This indicates that linear lift affects the flag's dynamics at this small aspect ratio. This finding is consistent with figure 2.7, where a difference is always observed between the $H/L \to 0$ theory of Section 2.1 and measurements at finite aspect ratio — even for the smallest aspect ratio of $H/L = 0.033$. As discussed, this mechanism acts in addition to twisting of the flag due to the combined effects of gravity and hydrodynamic loading, which leads to a reduction in deflection.

2.3 Conclusions

This chapter has addressed the behavior of slender (AR<1) inverted flags. Their stability has been shown to be remarkably different from that of their high aspect ratio counterpart. While the latter exhibits a divergence instability as flow speed increases, the undeformed state of an infinitely slender inverted flag is always locally stable. A saddle-node bifurcation emerges at finite flow speed, giving rise to two equilibrium states, with the more strongly deflected one being stable and the weakly deflected one unstable. The unstable equilibrium defines the boundary of the basin of attraction for the undeflected flag, which vanishes in the limit of high flow speed. The slender inverted-flag theory can be combined with that for large aspect ratio (Sader et al., 2016a), to yield a single formula for stability of the zero-deflection equilibrium, (2.10), that is valid for all aspect ratios.

Experimental measurements of inverted flags were performed and compared to theory, confirming he existence of multiple stable and unstable equilibria and the presence of intermittent dynamics. The experiments saw a significant twisting deformation that modified the position of the equilibria, as well as oscillations around the equilibrium positions. The presence of a saddle-node bifurcation was observed for aspect ratios up to 1.7. Inverted flags of small but finite aspect ratio were shown to present a combination of characteristics of both linear and quadratic fluid force dynamics.

The behavior of inverted flags of small but finite aspect ratios has been addressed in detail in a follow-up theoretical investigation by Tavallaeinejad et al. (2018), who solved the beam equation in combination with the full potential flow theory of Bollay (1939) (without taking the AR $\rightarrow 0$ limit) using a Hamiltonian framework. Their results show good agreement with the experimental measurements reported in Section 2.2. Interestingly, they studied the effect of a small non-zero initial curvature of the plate, which is applicable to all experimental measurements, and highlighted that the zero deflection equilibrium of those plates becomes unstable at finite velocity even for the AR$\rightarrow 0$ limit.